




## Vibroequilibria in microgravity: Comparison of experiments and theory

P. Salgado Sánchez <sup>\*</sup>, J. Fernández , I. Tinao, and J. Porter 

*Center for Computational Simulation, Escuela Técnica Superior de Ingeniería Aeronáutica y del Espacio, Universidad Politécnica de Madrid, Plaza de Cardenal Cisneros 3, 28040 Madrid, Spain*



(Received 24 July 2019; revised manuscript received 24 October 2019; published 10 December 2019)

Experiments on vibrated fluids confined in cylindrical and cuboidal containers were performed under the reduced gravity conditions of a parabolic flight. The results constitute a systematic quantitative investigation of the vibroequilibria effect, which refers to the reorientation of vibrated fluids in response to the inhomogeneous oscillatory velocity field and the accompanying dynamic pressure. This effect is amplified in microgravity where the restoring force of gravity is small or absent. Here the vibrations are transmitted via a pair of piezoelectric ceramics and a cantilever beam, excited in a resonant mode. The first and second resonances exhibit different types of motion and lead to different types of vibroequilibria surfaces, one with a dip or crater in the interior and the other flattened compared to the unforced reference experiment. The general tendency for interfaces to orient more perpendicular, on average, to the vibrational axis is confirmed. In the case of water in a cuboidal container, a quantitative comparison is made with vibroequilibria theory and with direct simulations of the Navier-Stokes equations. The good agreement confirms the predictions of vibroequilibria theory and suggests the capacity of this phenomenon to manipulate and position fluids in space environments through the choice of frequency and resonant mode.

DOI: [10.1103/PhysRevE.100.063103](https://doi.org/10.1103/PhysRevE.100.063103)

### I. INTRODUCTION

By nature, fluids move easily in response to external forces and the ability to manage and control this motion is a crucial aspect of wide-ranging applications in physics, chemistry, biology, medicine, and engineering. While small volumes of fluid may often be effectively manipulated using capillary effects, electromagnetic fields, or acoustic forces, this becomes increasingly difficult for larger volumes of liquid, whose distribution is dominated by gravity. Density stratification to minimize gravitational energy is a near-universal feature of fluid configurations larger than the capillary length scale and, among other things, explains the familiar sight of flat liquid-air interfaces on Earth.

In microgravity environments, on the other hand, fluid behavior is different. Surface tension and contact forces come to the fore and largely determine the shape and location of any free interfaces. A floating mass of liquid will minimize its surface energy by taking a spherical shape, while adhesive forces may cause it to wet a solid boundary on contact. The increased ease with which fluids can move (vertically) in microgravity, and the preference for curved hydrostatic interfaces rather than flat ones, means that fluid management is substantially more complicated than it is on Earth. At the same time, large-scale manipulation of fluids may become more feasible when gravity is no longer the limiting factor.

Vibrations are an inherent feature of most real environments, with their importance for a given physical process depending on amplitude, frequency, and orientation. Even in the simple case of purely periodic motion, they can affect a

range of important fluid phenomena such as mixing [1] and mass transfer.

If there is an interface separating fluids of different density, vibrations will generally excite waves. The vibrating motion of a solid support or boundary generates harmonic (synchronous) waves that decay, due to viscous effects, as they travel inward. At a critical amplitude, subharmonic waves (having twice the period of the vibrational forcing) may be excited via a parametric forcing mechanism arising from the oscillating pressure gradient [2,3]. If the source of this parametric forcing is localized, as it is near a side wall in a horizontally vibrating open container of liquid, then the subharmonic waves are similarly localized and are commonly known as cross-waves [4–7]. On the other hand, if the motion is vertical, perpendicular to the unperturbed flat interface, then the forcing is homogeneous and produces subharmonic Faraday waves [8–10] across the entire domain.

In addition to standing or traveling waves, vibrations parallel to an interface separating fluids of different density can drive a Kelvin-Helmholtz-type instability producing quasissteady, or “frozen,” waves [11–13]. These frozen waves are initially sinusoidal in form and grow as the amplitude of vibrations increases. As with oscillatory disturbances like Faraday waves and cross-waves, they may be considered, in the usual supercritical case near onset, as perturbations of the initial flat interface. This is no longer so without the restoring force of gravity. In weightlessness, the frozen waves rapidly develop into large-scale columnar structures with alternating (nearly) vertical interfaces [14,15]. Recent microgravity experiments [16,17] have shown that Faraday waves can subsequently be excited on these columnar interfaces to create a complex structure with two characteristic wavelengths. The pattern selection process is mainly controlled by vibrational velocity but is affected by viscosity [13] and finite-size effects [18].

<sup>\*</sup>pablo.salgado@upm.es

The example of frozen waves illustrates the dramatic effect that even small-amplitude vibrations can have in microgravity. In contrast to the situation on ground, they can lead to a large-scale redistribution of the liquids involved and, in so doing, facilitate a secondary Faraday wave instability that would not otherwise occur. It is not necessary to have the frozen wave (Kelvin-Helmholtz) instability for such a redistribution to happen either. The inhomogeneous oscillatory velocity field is naturally accompanied by an inhomogeneous dynamic pressure that drives a reorientation of the fluid. This phenomenon, known as the vibroequilibria effect, was observed by Faraday [8] in the flattening of drops beneath a vibrating plate. Ordinary gravity masks the vibroequilibria effect for most common fluid configurations (unless very large forcing is applied), while in microgravity environments, vibrations compete only with surface tension and contact forces so their effect is greatly enhanced.

The usual theoretical approach to vibroequilibria [19–21] assumes a separation of timescales between the high-frequency forcing and the slower viscous diffusion of momentum. If the flow is further assumed to be potential, then a variational method can be used to determine the quasisteady equilibrium of the surface as the critical point of a Lagrangian averaged over the fast timescale.

A recent investigation [22] compared vibroequilibria theory with direct numerical simulations and found good agreement over a range of parameters. It was further demonstrated that, depending on fluid depth, the symmetric vibroequilibria solution in a horizontally vibrated rectangular container can disappear in a saddle-node bifurcation, after which the surface dips violently toward the lower boundary and undergoes a disordered transition to one of many possible asymmetric states. In low-viscosity fluids, surface waves can interact with the underlying vibroequilibria state and may even destabilize it through excitation of the first odd sloshing mode; this is likely related to the presence of temporal modulations resulting from the interaction between subharmonic wave fields emanating from opposite sides of the container [3,23,24].

The first experimental observation of the vibroequilibria effect in confined fluids was by Wolf [11], who applied large-amplitude vibrations (936 mm/s) to a 60-mm-long cylindrical container of diameter 28 mm holding an aqueous solution of potassium iodide and a lighter oil (SAE 140). In microgravity, the only prior vibroequilibria experiment that we are aware of was conducted by Ganiev *et al.* [25], who investigated combinations of water, oil, and air in the reduced gravity of a parabolic flight. Partially filled cylinders of length 100 mm and diameter 30 mm were vibrated at low frequencies (8 Hz, 12 Hz), producing disordered dynamics, and at high frequencies (600–800 Hz), where deep funnels or craters were seen for the air-water interface near a resonance frequency. This behavior, which is now recognized as indicative of the vibroequilibria effect in horizontally vibrated containers [22], was only later shown [21] to be qualitatively consistent with vibroequilibria theory and was not quantitatively compared with either theory or simulations.

A more systematic experimental investigation of vibroequilibria solutions and their importance in microgravity is called for, not only for the potential observation of novel states like those mentioned above, but for their ability to

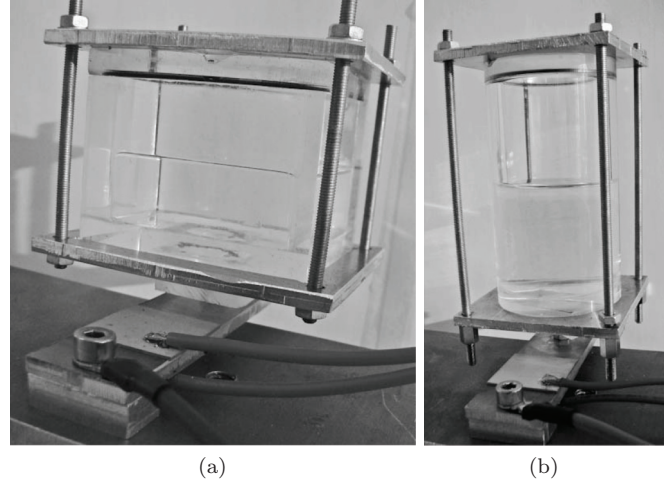


FIG. 1. Pictures of the experimental cells and the bender beam: (a) cuboid and (b) cylinder. The cells are held closed by four bolts, which compress the PMMA body and cover against an O-ring. The aluminum bender beam has two piezoelectric ceramics attached to opposite horizontal faces. Cables associated with electrical excitation of the ceramics and the clamping bolt can also be seen.

manipulate fluids in weightless environments. Indeed, vibrations are known to mimic the effect of gravity in certain aspects of convection and phase transitions [26] and vibroequilibria can be regarded in this light too. The general tendency, with increasing forcing, is for the vibroequilibria states to develop so that large portions of the surface are nearly perpendicular to the axis of vibration, reminiscent of how fluid surfaces align perpendicular to gravity.

With this motivation, the behavior of fluids in microgravity and the potential for controlling them through the vibroequilibria effect were investigated in the Control of Fluids in microgravity with Vibrations (CFVib) experiment [27], which looked at representative liquid-gas and two-liquid combinations in rectangular cuboidal and cylindrical containers excited by periodic vibrations and was performed during the 65th ESA Parabolic Flight campaign. The vibroequilibria effect was measured as a function of forcing amplitude at different resonance frequencies having different characteristic modes of vibration.

In this paper, we present the main scientific results obtained during the CFVib experiment and compare them to theoretical predictions. The experimental setup is described in Sec. II. The mathematical formulation used in the numerical simulations is given in Sec. III, together with a basic review of vibroequilibria theory. The most relevant results of the experiment are presented in Secs. IV and V, while the case of water in a cuboidal container is quantitatively compared both to direct numerical simulations and to vibroequilibria theory in Sec. VC. Conclusions are provided in Sec. VI.

## II. THE EXPERIMENT

The experiment is designed to compare pairs of cuboidal and cylindrical cells (see Fig. 1) containing a liquid-air or immiscible two-liquid combination (the latter is not described here since the experimental results were inconclusive). One of

TABLE I. Characteristic physical properties of the experimental liquids at room temperature: density  $\rho$ , surface tension  $\Gamma$ , and kinematic viscosity  $\nu$ . These values are used in the mathematical simulations using the formulation of Sec. III.

	$\rho$ (kg/m <sup>3</sup> )	$\Gamma$ (N/m)	$\nu$ (m <sup>2</sup> /s)
Water	1000	$7.20 \times 10^{-2}$	$1 \times 10^{-6}$
50-cSt silicone oil	960	$2.08 \times 10^{-2}$	$50 \times 10^{-6}$

the cells is subjected to vibrations at various amplitudes and frequencies, while the reference cell is unforced and responds only to the residual acceleration present on the parabolic flight. These two simple geometries, which represent common fluid containers, can be expected to lead to different interfacial dynamics. In addition, the use of cuboidal cells has the advantage that (quasi) two-dimensional behavior can be assumed in some cases, while the cylindrical cells can be compared with the previous observations of Ganiev *et al.* [25].

The containers are made of transparent polymethyl methacrylate (PMMA) to allow for visualization of the liquid interface. The cuboids are 30 mm  $\times$  40 mm  $\times$  30 mm (length  $\times$  width  $\times$  height), while the cylinders have an interior radius of 15 mm and a height of 60 mm. Each cell is composed of two PMMA pieces that are held against each other using bolted aluminum plates and sealed with an O-ring; part of this can be seen in Fig. 1. The results described here are obtained with water and 50-cSt silicone oil, whose relevant properties are given in Table I.

Each experimental cell is fixed to an aluminum beam (cantilever) that, in the case of the excited cells, has two piezoelectric ceramics (PZTs), attached on opposite horizontal faces. An alternating counterphase voltage is applied to each PZT after being boosted by an amplifier. The counterphase mechanical stress induced in the ceramics creates a torque that drives periodic flexural motion of the beam and shakes the cell.

Both the amplitude  $V$  (with a maximum determined by the amplifier) and frequency  $f$  of the applied voltage can be varied to control the magnitude and characteristics of the vibrations. The experiments use voltages up to 100 V, while the frequencies are selected to match the most relevant resonant modes of the assembly. The first and second resonances (at approximately 80 and 215 Hz, respectively, for the cuboids) were found to be associated with the largest displacements and, therefore, the most pronounced vibroequilibria effects. Accelerometers directly measure the (vertical) acceleration on each vibrated container.

Although the motion of the container induced by the PZTs in a bender-beam configuration is not purely linear (see Sec. III for more details), combining translational motion with some degree of rotation, it has the advantage of small size and low power (compared to an electromagnetic shaker, for example). The selected transducer yields significantly higher amplitudes for a given voltage than alternative configurations (such as a bclamped beam), at least for the resonant modes excited here.

The optical system that monitors the position of the fluid includes a complementary metal-oxide-semiconductor

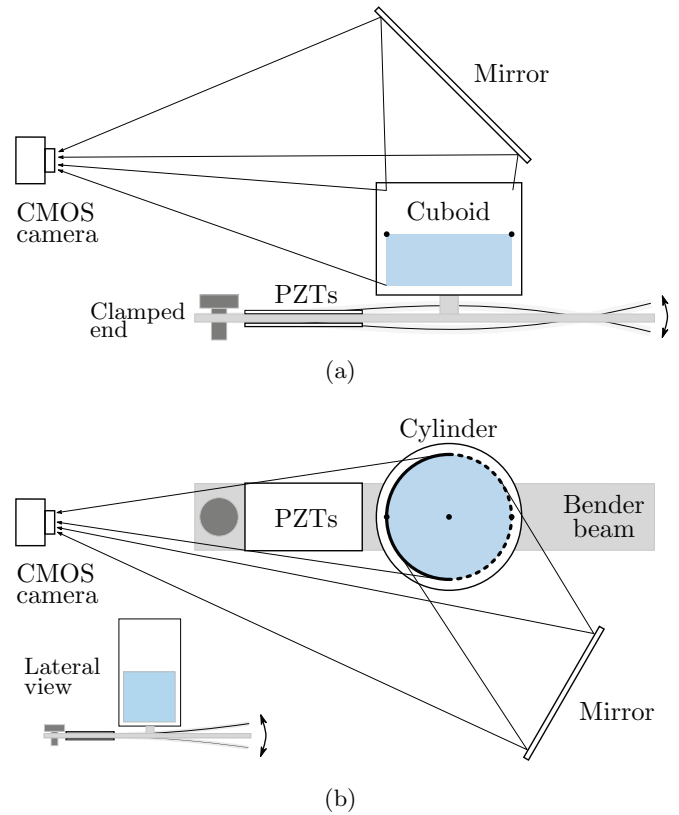


FIG. 2. Sketch of experimental setup with (a) cuboid and (b) cylinder. Shown are the (partially filled) experimental cell, bender beam, piezoelectric ceramics, mirror, and CMOS camera. Selected optical paths indicate the direct and reflected images referred to in later sections. The inset in (b) shows a lateral view of the setup for a cylindrical cell. Shaded curves illustrate the excited motion of the beam for the first (b, inset) and second (a) resonant modes.

(CMOS) camera, a mirror, and a source of illumination. For the vibrated cells, the CMOS sensor samples at (approximately) 20 frames per second, providing excellent resolution of the slow timescale dynamics of the surface; the reference cells were recorded at (approximately) 10 frames per seconds. The behavior of the liquid surface was observed along the axis of the beam and after reflection by a mirror. Depending on the cell geometry, this mirror provides either a top view (for the cuboidal cell) or a lateral view (for the cylindrical cell). Both experimental setups are sketched in Fig. 2, which shows the container, bender beam, PZTs, CMOS camera, and mirror. Selected optical paths are drawn to illustrate the direct and reflected (top or lateral) views. Included illustrations indicate the dominant type of motion for the first resonant mode [see the inset in Fig. 2(b)] and the second one [Fig. 2(a)].

Experiments were performed under the reduced gravity provided by a parabolic flight [28], which lasts approximately 20 s. The microgravity level (residual acceleration) during the parabolic maneuvers was measured by the onboard accelerometers and provided each day by the airplane operators [29]. This microgravity level satisfied

$$|g_z| \lesssim 0.05 g_0, \quad |g_{x,y}| \lesssim 0.01 g_0, \quad (1)$$

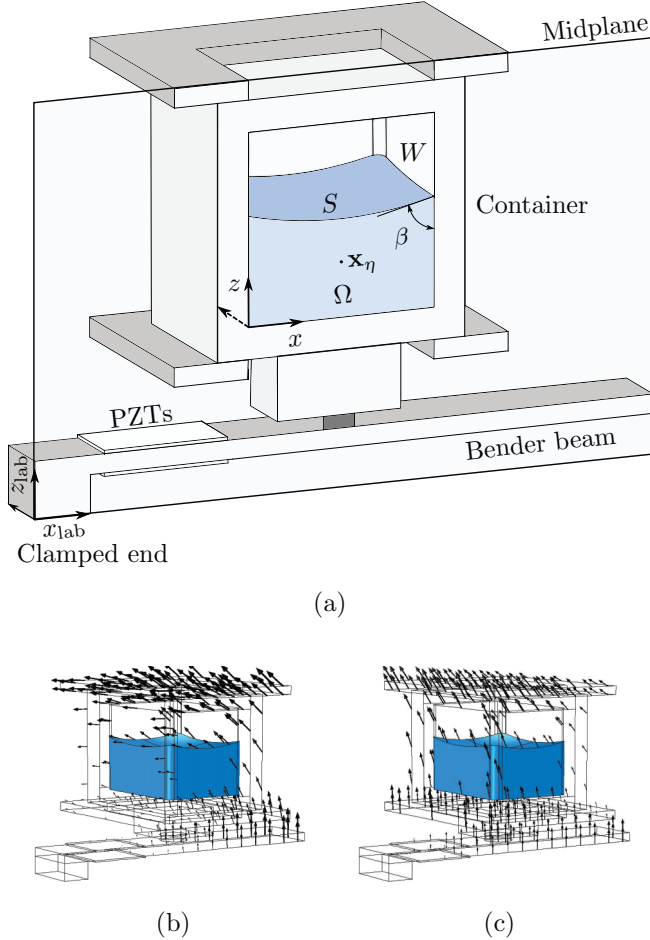


FIG. 3. (a) Midplane cut of the experimental setup for a cuboidal container showing the bender beam, PZTs, fluid volume  $\Omega$ , free surface  $S$ , and solid boundaries  $W$ . The container and laboratory reference frames are illustrated; since the displacement is very small compared to the container size, we assume hereafter that  $(x, y, z) \simeq (x_{\text{lab}}, y_{\text{lab}}, z_{\text{lab}})$ . This geometry is used for the numerical results shown in Sec. VC. The motion associated with the first two resonant modes is illustrated in (b) and (c), respectively.

where  $g_0 = 9.81 \text{ m/s}^2$ . The components are expressed in the airplane reference frame [28], defined by axes  $\tilde{x}$ , oriented aft to front;  $\tilde{y}$ , oriented along the wings; and  $\tilde{z}$ , perpendicular to the floor and identical to the vertical  $z$  axis of the container (see Fig. 3). The cuboidal containers are aligned, approximately, with the airplane axes so that  $(x, y) \approx (-\tilde{y}, \tilde{x})$ , while the cylindrical containers are rotated by approximately  $45^\circ$  (clockwise) with respect to the longitudinal axis of the plane.

In this paper, we highlight the results observed in microgravity with the cylindrical cells when vibrated in the first resonant mode and the cuboidal cells when vibrated in the first and second resonant modes. For further details about the experiment, see Ref. [27], where a review of the design, implementation, and execution is given.

### III. MATHEMATICAL FORMULATION

We consider a finite volume of fluid  $\Omega$  (see Fig. 3) with a free surface held in a container in the presence of a gravita-

tional field and subjected to vibrations of frequency  $\omega$ . The fluid satisfies the incompressible Navier-Stokes momentum and mass continuity equations [30]

$$\mathbf{u}_t + (\mathbf{u} \cdot \nabla) \mathbf{u} = -\nabla p + \nu \Delta \mathbf{u} + \mathbf{G}(\mathbf{x}, \mathbf{u}, t), \quad (2a)$$

$$\nabla \cdot \mathbf{u} = 0, \quad (2b)$$

where  $\mathbf{u}$  is the velocity,  $\rho$  is the density,  $\nu$  is the kinematic viscosity, and  $p$  is the pressure.

The inhomogeneous acceleration  $\mathbf{G}(\mathbf{x}, \mathbf{u}, t)$ , which is expressed in the accelerating frame of the container, can be written, to leading order, as

$$\begin{aligned} \mathbf{G}(\mathbf{x}, \mathbf{u}, t) = & \mathbf{g}(t) + \omega \mathbf{v}_\eta \cos(\omega t) + 2\boldsymbol{\omega} \times \mathbf{u} \\ & + \boldsymbol{\omega} \times [\boldsymbol{\omega} \times (\mathbf{x} - \mathbf{x}_\eta)] + \dot{\boldsymbol{\omega}} \times (\mathbf{x} - \mathbf{x}_\eta), \end{aligned} \quad (3)$$

where  $\mathbf{g}(t)$  is the time-dependent residual gravity field in the parabolic flight environment,  $\mathbf{v}_\eta$  is the (approximately) linear velocity of a reference point  $\mathbf{x}_\eta$ , taken here to be the center of the unperturbed fluid (see Fig. 3), and  $\boldsymbol{\omega}(t)$  is the rotational velocity of the container about that reference point. Both the linear and rotational motion are assumed to lie in the  $(x, z)$  plane defined in Fig. 3. The magnitude of the rotational velocity  $|\boldsymbol{\omega}(t)| = \omega_0 \sin(\omega t)$  depends on the mode of vibration and the forcing amplitude, but  $\omega_0$  is typically on the order of 1 rad/s.

Navier-slip boundary conditions [18] are imposed on the solid boundaries  $W$  to preserve the contact angle  $\beta$  and allow for motion of the contact line. The balance among surface tension, pressure, and viscous stresses holds at the free surface  $S$  defined by  $f(\mathbf{x}, t) = 0$ ,

$$\mathbf{u} \cdot \mathbf{n}_w = 0 \quad \text{on } W, \quad (4a)$$

$$p \mathbf{n} - \left( \frac{\Gamma}{\rho} \right) \kappa \mathbf{n} - \nu (\nabla \mathbf{u}) \cdot \mathbf{n} = 0 \quad \text{on } S, \quad (4b)$$

$$f_t + \mathbf{u} \cdot \nabla f = 0 \quad \text{on } S. \quad (4c)$$

Here  $\kappa$  is the mean curvature of the interface  $f(\mathbf{x}, t) = 0$  defined as

$$2\kappa(f) = \nabla \cdot \left( \frac{\nabla f}{|\nabla f|} \right), \quad (5)$$

and  $\mathbf{n} = \nabla f / |\nabla f|$  is a unit normal vector.

In Sec. VC, we compare experiments with the solution of Eqs. (2)–(5) in a two-dimensional domain. We also compare with established vibroequilibria theory, which is summarized below.

#### A. Vibroequilibria theory

The theory of vibroequilibria [19–21] provides a method for calculating the quasisteady (average) equilibrium states of a fluid configuration with a free interface. It assumes a separation of timescales between the forcing at frequency  $\omega$  and the slower (averaged) response of the fluid, characterized by the viscous timescale  $L^2/\nu$ , and the period of the primary sloshing modes [20,21]; if incompressibility is assumed, then this further requires the forcing frequency to be below the first acoustic resonance.

A variational approach using a time-averaged Lagrangian casts the problem as one of determining critical points for



a functional that depends on the shape of the interface. For this step, it is further assumed that the leading-order velocity field is potential, with  $\mathbf{u} = \nabla\phi$ , and varies harmonically at the frequency of the applied forcing:

$$\phi(\mathbf{x}, t) = v_\eta \tilde{\phi}(\mathbf{x}) \cos(\omega t) + \dots \quad (6)$$

The free surface is split into oscillatory and average parts,

$$f(\mathbf{x}, t) = \tilde{F}(\mathbf{x}) + \tilde{f}(\mathbf{x}) \cos(\omega t) + \dots \quad (7)$$

Note that rotational motion of the container is not generally compatible with potential flow. Of the three rotational contributions in Eq. (3), it is typically the final term (the Euler acceleration) that is the largest for the resonant modes of interest. For these excitations, none of the rotational terms are as large as the linear acceleration  $\omega v_\eta$ , which justifies neglecting them at leading order so that the standard (variational) approach to vibroequilibria theory can be used; the error this introduces is discussed in Sec. V C.

If there is a constant gravitational acceleration  $g$  taken to be aligned with the vertical  $z$  axis (see Fig. 3), then the vibroequilibria defined by the surface  $\tilde{F}(\mathbf{x}) = 0$  is dynamically stable if it is a local minimum of the time-averaged functional [20,21],

$$\begin{aligned} \mathcal{L} = \int_{(\Omega)} \left( gz + \frac{v_\eta^2}{4} |\nabla \tilde{\phi}|^2 + P_0 \right) d\Omega \\ + \frac{\Gamma}{\rho} \int_{(S)} dS - \frac{\Gamma}{\rho} \sin \beta \int_{(W)} dW, \end{aligned} \quad (8)$$

where  $P_0$  is a Lagrange multiplier for enforcing conservation of volume. The functional (8) should be minimized over permissible configurations of  $\tilde{F}(\mathbf{x})$ . Assuming the surface can be expressed as a single-valued function  $z = F(x, y)$  and using the rescalings

$$\mathbf{x} \rightarrow L\mathbf{x}, \quad P_0 \rightarrow \frac{\Gamma}{\rho L} P_0, \quad \tilde{\phi} \rightarrow L\tilde{\phi}, \quad \mathcal{L} \rightarrow \frac{\Gamma L^2}{\rho} \mathcal{L}, \quad (9)$$

the functional can be rewritten (see Ref. [22] for details) as

$$\begin{aligned} \mathcal{L} = P_0 \mathcal{V} + \int_S dS + \eta \int_S (\mathbf{e} \cdot \mathbf{x}) q(\mathbf{x}) dS \\ - \sin \beta \int_W dW + \frac{\text{Bo}}{2} \int_S [F(x, y)^2 - d^2] dx dy, \end{aligned} \quad (10)$$

where  $d$  is the liquid depth with a flat horizontal surface and  $q(\mathbf{x}) = \partial \tilde{\phi} / \partial n$ . The nondimensional parameter,

$$\eta = \frac{\rho L}{4\Gamma} v_\eta^2, \quad (11)$$

characterizes the ratio of vibrational energy to surface energy, while the Bond number,

$$\text{Bo} = \frac{\rho L^2}{\Gamma} g, \quad (12)$$

characterizes the relative importance of gravitational and surface energy. We minimize Eq. (10) using the boundary element method, as in Ref. [22], to obtain the predicted vibroequilibria surface.

#### IV. VIBROEQUILIBRIA IN A CYLINDRICAL CONTAINER

Figure 4 shows the evolution of the fluid surface in three vibrated cylindrical containers approximately half-filled with silicone oil, to be compared with the unforced reference cell (top row). In each experiment, the free surface is captured from the front and from a lateral view and is illustrated at three different times (labeled in the figure) measured with respect to the beginning of the excitation in microgravity at  $t = 0$  s. These snapshots are selected to show the liquid surface at the beginning of the excitation, at the time when the contact line reaches the upper lid of the container (or its maximum height), and at an intermediate point between these.

The vibrations are delivered at a fixed frequency  $f = 59.3$  Hz, which corresponds to the first resonant mode, and for three applied voltages of 80, 90, and 100 V; these give vertical vibrational velocities  $v_z$  (measured at the accelerometer) of 73.9 [Figs. 4(a)–4(c)], 84.6 [Figs. 4(d)–4(f)], and 94.8 mm/s [Figs. 4(g)–4(i)], respectively. For the experiment shown in Figs. 4(a)–4(c), each snapshot of the vibrated cell is shown below a corresponding snapshot of the reference cell. The front and rear halves of the contact line are highlighted in solid and dashed lines, respectively, as a visual reference. Recall that the lateral views are obtained after reflection, as illustrated in Fig. 2.

The experiments shown in Fig. 4 are quantified in Fig. 5, where the uppermost (solid dots) and lowermost (diamonds) visible points of the surface, which are located along the contact line and in the interior, respectively, are shown as a function of time. The vibrated surface (marked in black) and the reference experiment (marked in gray) can be compared. Each plot is shown above the corresponding residual gravity measurement, given in the airplane reference frame. The vertical vibrational velocities  $v_z$  measured by the accelerometer of 73.9 (a), 84.6 (b), and 94.8 mm/s (c) are indicated, as are the times (shown with vertical lines) of the snapshots included in Fig. 4.

Prior to the beginning of the excitation in microgravity, the equilibrium reflects a balance between residual gravity and contact forces. Since silicone oil easily wets most surfaces and has a low contact angle, the surface resembles a spherical cap; see Figs. 4(a), 4(d) and 4(g). In the absence of applied vibrations, this spherical caplike shape is maintained throughout the experiment, although it responds with some degree of motion to the changing residual gravity, as seen in the snapshots of the reference cell in Figs. 4(a)–4(c). Applied vibrations, in contrast, modify this interface shape significantly.

Immediately after the forcing is initiated, the fluid moves toward a new (quasisteady) equilibrium, evolving on a slow timescale compared to the forcing period. This vibroequilibria effect is quantified by recording the motion of the contact line with respect to the minimum height of the visible surface, which occurs in the interior. What is generally observed with increasing amplitude is the gradual upward motion of the “front” and “rear” halves of the contact line, as seen in Figs. 4 and 5. This movement of the surface, which is driven by the spatially inhomogeneous vibrational velocity field, is affected by the residual gravity level. In particular, there is an evident correlation with the vertical gravity component (black curve

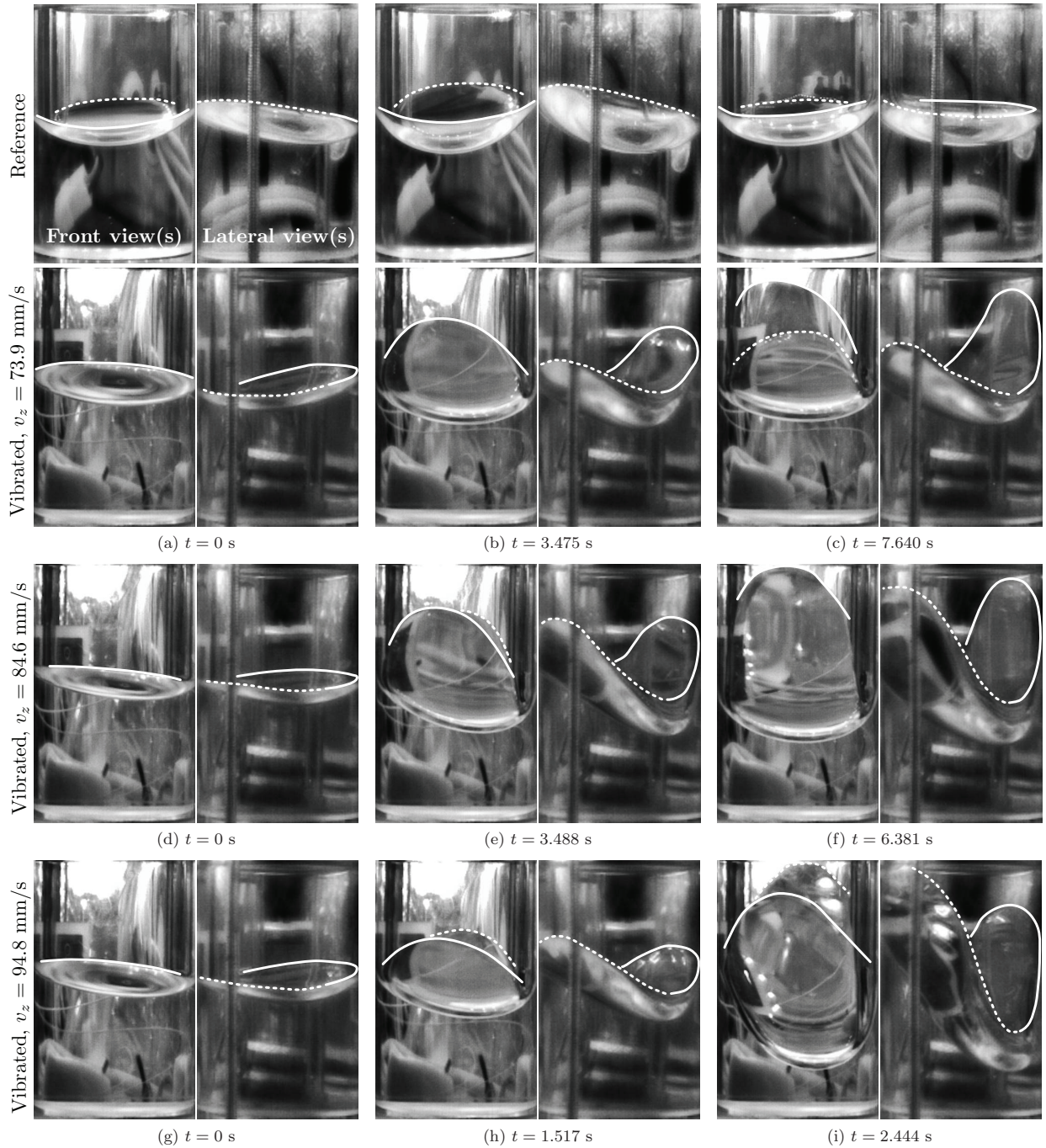


FIG. 4. Snapshots (front and lateral views) showing the evolution of the surface of silicone oil in a cylindrical cell. The upper row of panels (a)–(c) shows the fluid behavior in the reference cell (experiencing residual acceleration of the airplane) at the given times, paired with corresponding snapshots of a vibrated experiment. The vibrated experiments are excited at  $f = 59.3$  Hz with vibrational velocities [(a)–(c)]  $v_z = 73.9$ , [(d)–(f)]  $84.6$ , and [(g)–(i)]  $94.8$  mm/s, which correspond to applied (peak) voltages of 80, 90, and 100 V, respectively. To help visualize the free surface deformation, contact lines at “front” and “rear” halves of the lateral wall are highlighted with solid and dashed lines.

in the lower panels of Fig. 5), reflecting the suppression of vibroequilibria effects for a given vibrational forcing with increasing gravity level (Bond number).

The interior of the free surface, on the other hand, tends to move downward per conservation of mass (see Figs. 4 and 5). Depending on the forcing amplitude, the contact line may reach the upper lid of the container, as with the experiments at  $84.6$  and  $94.8$  mm/s [Figs. 5(b) and 5(c) and Figs. 4(f) and 4(i)] or stop prior to that, as with the experiment at  $73.9$  mm/s

[Fig. 5(a) and Fig. 4(c)]. For the experiments where the contact line reaches the top of the container, the effect of increasing vibrational amplitude is reflected in the time required for the fluid to arrive at that boundary. This contact time, which decreases from  $6.38$  s for  $v_z = 84.6$  mm/s to  $2.44$  s for  $v_z = 94.8$  mm/s, is also affected by the residual gravity level. Generally, the effect of (vertical) gravity is to flatten the surface; a higher vertical gravity level thus requires greater applied forcing to achieve a similar vibroequilibria effect.

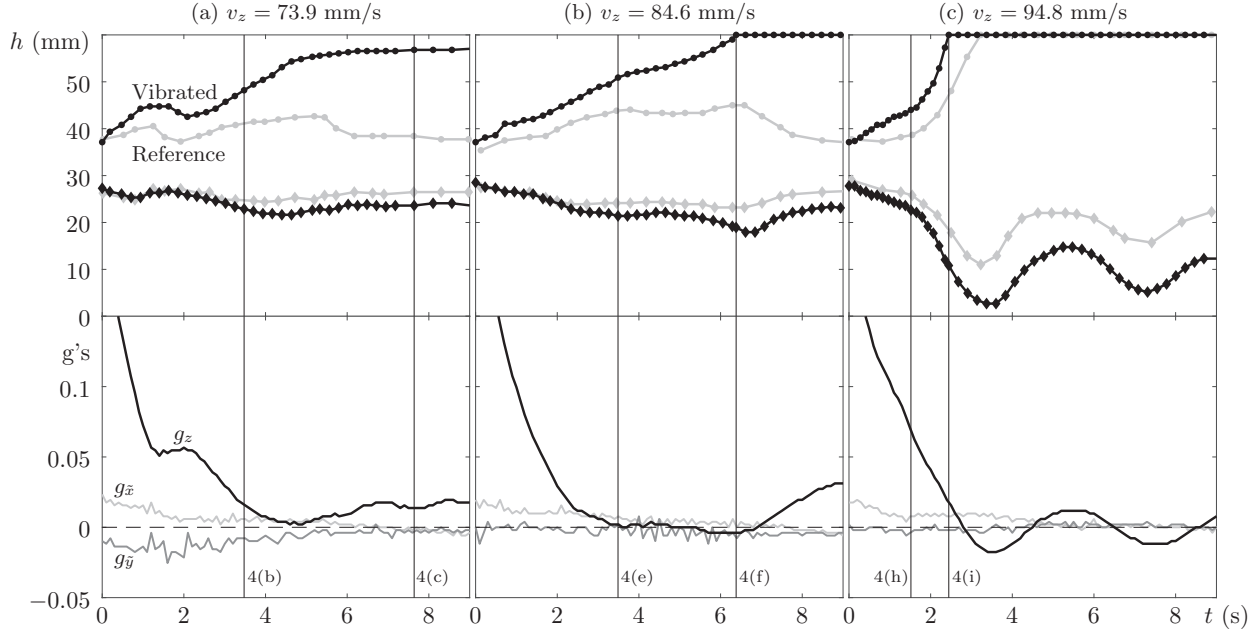


FIG. 5. Evolution in time of the highest visible point of the contact line (solid dots) and the minimum visible point of the fluid surface (diamonds) in vibrated (black) and reference (gray) cells. Vibrations are delivered at  $f = 59.3$  Hz and different applied vibrational velocities: (a)  $v_z = 73.9$ , (b)  $84.6$ , and (c)  $94.8$  mm/s, which correspond to applied (peak) voltages of 80, 90, and 100 V, respectively. Measurements of the residual gravity level are shown below each panel, with the labeled components measured in the airplane reference frame. Vertical lines mark the times when the snapshots in Fig. 4 are taken [labeled as 4(b), 4(c), 4(e), 4(f), 4(h), 4(i)].

Although the vibrations induced by the first resonant mode of the beam are oblique [see Fig. 3(b)], the observed vibroequilibria is relatively symmetric. In this aspect, the vibroequilibria surface recalls the case of horizontally vibrated containers [22], suggesting that the horizontal component is dominant. These results are also qualitatively consistent with the experiments of Ganiev *et al.* [25], which found a similar cratering of the interior surface in vibrated cylindrical cavities.

A similar, but much smaller, vibroequilibria effect was found in the cylindrical cell that was half-filled with water. This is likely explained by the fact that water has a higher surface tension and contact angle than oil, so the barrier for vibrational energy to overcome surface and contact energy is greater [see Eq. (10)]. In addition, the reduced viscosity of water allows the earlier excitation of surface waves. At the highest voltages, these waves are of high amplitude and drive the ejection of drops [31,32]. This drop ejection process has recently been analyzed experimentally with vibrated immiscible liquids in microgravity [17], where the interfacial energy was measured with increasing amplitude and found to be consistent with the scaling suggested by vibroequilibria theory via Eq. (10); the interfacial energy of the drops increases as the square of the dimensionless vibrational velocity, or  $\eta$ , measured relative to the drop ejection threshold.

## V. VIBROEQUILIBRIA IN A CUBOIDAL CONTAINER

Here we consider the experiments in the cuboidal container holding either silicone oil or water. For the latter case, the experimental results are quantitatively compared with simulations of the Navier-Stokes equations and with vibroequilibria theory.

### A. Experiments with silicone oil

Figure 6 provides front and top views showing the evolution in time of silicone oil in a cuboidal container. The fluid behavior in the reference cell (upper two rows of snapshots), which is affected by the residual gravity in the airplane, and the vibrated cell (lower two rows of snapshots) can be compared at the same times. The vibrated cell is driven in the first resonant mode of the beam at  $f = 83.07$  Hz and  $v_\eta = 161.6$  mm/s, which corresponds to an applied peak voltage of 100 V. When they are clearly visible, the “front” and “rear” contact lines are highlighted using solid and dashed lines, respectively.

In contrast to the results of Sec. IV, when enough silicone oil is present, a bubble develops in the cuboidal container (see the upper row of Fig. 6). This bubble persists throughout the microgravity period, although its location and shape vary somewhat due to residual gravity. We attribute the appearance of this bubble in the cuboidal container (and its absence in the cylindrical one) both to geometry—the cuboidal cells have lateral corners, which facilitate wetting and capillary action, and they are half as high as the cylindrical cells, so the fluid can more easily reach the upper lid—and to the different roughness of the PMMA walls resulting from the distinct manufacturing procedures used. This roughness, which is assumed to be greater in the case of the cuboidal cells, can significantly modify the contact line dynamics.

In general, the contact line dynamics depend on surface properties and on forcing. Without forcing, meniscus effects extend, for a representative residual gravity of  $g = 0.05 g_0$ , over the length scale  $l_c \sim \sqrt{\Gamma/(\rho g)} \approx 12$  mm (water) and 7 mm (silicone oil). The fact that the capillary length is comparable to the container size explains the curvature observed



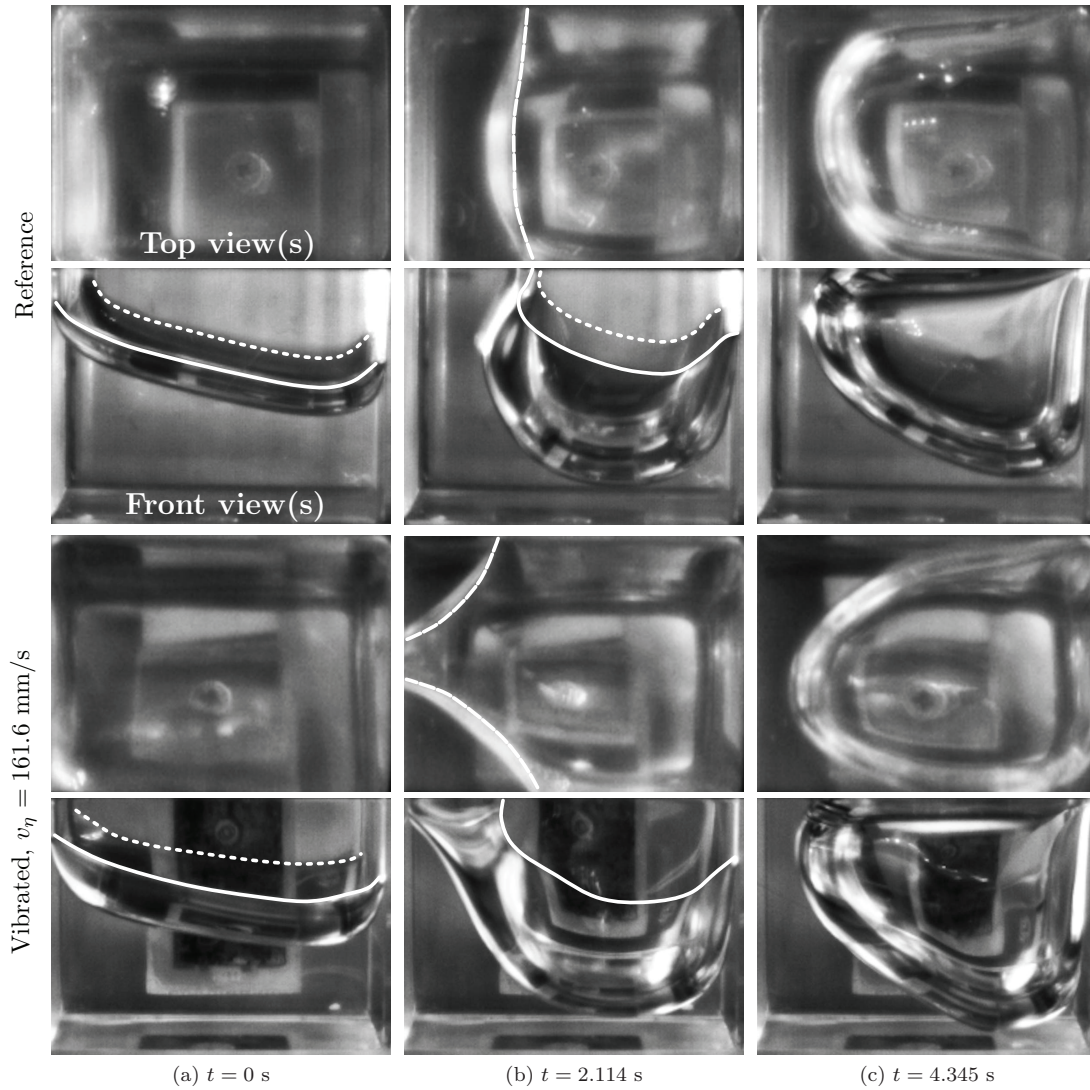


FIG. 6. Snapshots (top and front views) showing the evolution in time of experiments with silicone oil in a cuboidal container. The upper two rows show the reference cell, which is subjected to the airplane’s residual gravity, while the lower two rows show the cell excited at  $f = 83.07$  Hz and  $v_\eta = 161.6$  mm/s, corresponding to a peak voltage  $V = 100$  V. When feasible, the contact lines along the front and rear walls (front view) are highlighted using solid and dashed lines, respectively, as is the contact line in the upper views.

in the reference cells during the microgravity portion of the flight (see Sec. VB). With forcing, the vibrational capillary length can be estimated [33] as  $l_c \sim \sqrt{\Gamma/(\rho A \omega^2)} \approx 1$  mm, where  $A$  and  $\omega$  are the vibrational amplitude and frequency, respectively. Meniscus effects are thus expected to have only a weak effect on the vibroequilibria solutions when the contact angle is relatively large, as with water. For silicone oil in cuboidal containers, however, strong capillary effects are observed even under applied vibrations, as is clear from the formation of the large air bubble in the interior.

The formation of a large bubble means that the effect of the applied vibrations is more subtle than in Sec. IV, but a vibroequilibria effect is clearly present, as demonstrated by the different location of the contact lines seen in the figure. The applied vibration changes the bubble from an approximately spherical to a more elliptical shape; compare the top view of the reference and vibrated cells in Fig. 6(c). To leading order, these vibrations flatten the surface and make it more

perpendicular to the dominant vibrational axis, as vibroequilibria theory predicts [22]. Similar behavior was observed in recent parabolic flight experiments with immiscible fluids [17], where the flattening of an initial droplike configuration was seen for vibrations initiated in microgravity.

The initial condition of the fluid surface can clearly play an important role in selecting the observed vibroequilibria solution, with an approximately flat surface developing in quite a different manner than a large bubble. Notwithstanding this dependence on initial topology, we find that the smaller variations of the initial surface characteristic of the parabolic flight platform do not noticeably affect the development of vibroequilibria—residual gravity, as mentioned earlier, is a far more important factor.

We note that other phenomena, like the frozen wave instability that arises in two-fluid systems vibrated parallel to the unperturbed interface, can be much more sensitive to initial conditions. It was recently demonstrated that in



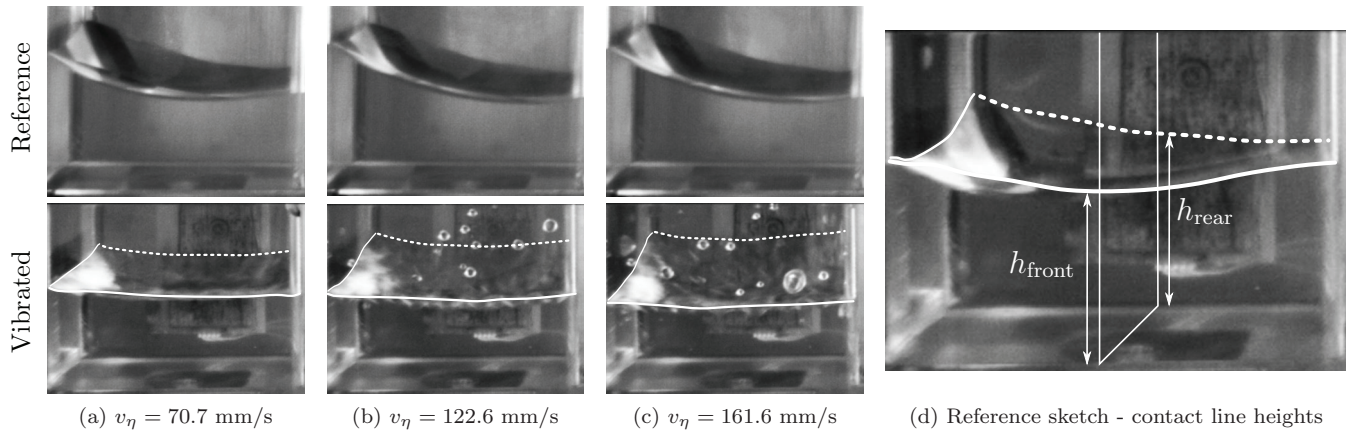


FIG. 7. [(a)–(c)] Snapshots of vibroequilibria in a cuboidal container vibrated at 79.8 Hz in the first resonant mode. Vibrational velocities are as follows: (a) 70.7, (b) 122.6, and (c) 161.6 mm/s, corresponding to peak voltages of 50, 80, and 100 V, respectively. The location of the “front” and “rear” contact lines is outlined with solid and dashed curves, respectively. Images of the reference cell at identical times are included for comparison. (d) Illustration of the measurement points used for quantitative comparison with the theory of Sec. VC.

similar microgravity experiments [34] the development of the frozen wave instability can be significantly affected, or suppressed, by a misalignment between the initial interface and the vibrational axis. In fact, to a large extent, this can be explained by the vibroequilibria effect and its ability to orient interfaces (density contours) perpendicular to the vibrational axis. Frozen waves do not affect the CFVib experimental results described here since the density of the upper fluid (air) is very low, making the frozen wave threshold [12,15] much higher than the forcing amplitudes used.

Experiments were also performed using 5-cSt silicone oil confined in both cuboidal and cylindrical cells, with a volume ratio of liquid to air of approximately 1/3 rather than 1/2. As discussed, the lower viscosity allows the same vibrational amplitude to excite higher-amplitude surface waves, which can trigger drop ejection, and this was observed with 5-cSt oil. Since there was less fluid volume than in the experiments with water, so less total mass, the vibrational amplitude (for a given applied voltage) was higher. This fact, along with the lower surface tension, led to a profusion of drops that, unfortunately, obscured the vibroequilibria effect. The final excited states were fully three dimensional and chaotic [17,31] and could not be effectively analyzed.

Compared to the results that follow in Secs. VB and VC, the experiments with silicone oil in a cuboidal container are more difficult to quantify and to compare directly with simulations or with theory. For one thing, the lateral motion of the bubble within the cuboidal cell makes the problem fully three dimensional, just as in the cylindrical cell. Accurate simulations would also require the treatment of topological changes in the fluid boundaries. Such a comparison between experiment and simulations is not attempted here.

## B. Experiments with water

Experiments performed in rectangular cuboidal containers with water provided good results both for the first and the second resonant modes. Results are discussed separately for each of these modes since the character of the vibrational motion is different, leading to distinct vibroequilibria.

### 1. First resonant mode

Figures 7(a)–7(c) show the vibroequilibria observed in three experiments at different vibrational velocities  $v_\eta$  of 70.7 (a), 122.6 (b), and 161.6 mm/s (c), corresponding to applied voltages of 50, 80, and 100 V, respectively. Snapshots of the reference cells at identical times are included for comparison.

The reference cells show (nearly) identical solutions, with the surface curved due to its contact angle and displaying a degree of leftward tilt due to the effect of residual gravity, particularly its component along the  $y$  axis (see Fig. 3), which approximately coincides with the  $\tilde{x}$  axis of the airplane; this scenario is similar to that of other recent parabolic flight experiments [17].

The vibroequilibria effect is revealed in the comparison between the excited and reference cells and can be quantified in terms of the contact line motion. Increasing the vibrational velocity (i.e., the applied voltage) causes the “front” contact line to move slowly downward, while the “rear” contact line climbs more rapidly upward. Consistent with conservation of volume, the interior portion of the surface dips downward at the same time, which makes this vibroequilibria qualitatively similar to previous solutions observed in the cylindrical container. In this case, however, the cratering is less pronounced, which suggests an effective vibrational axis that is, on average, more oblique.

As discussed above, the low viscosity of water facilitates drop ejection [17,31], which occurs when the forcing is large enough to excite high amplitude waves that rupture the surface [see Figs. 7(b) and 7(c)]. Generally, we observe drops of increased size in microgravity compared to hypergravity, consistent with the work of James *et al.* [31]. For a given vibration amplitude above threshold, this drop ejection is observed regardless of the initial conditions, as in Li and Umemura [35].

### 2. Second resonant mode

Figure 8 shows two snapshots of the water surface in a cuboidal container and allows the excited cell (lower row) to be compared with the unexcited reference cell (upper row) at

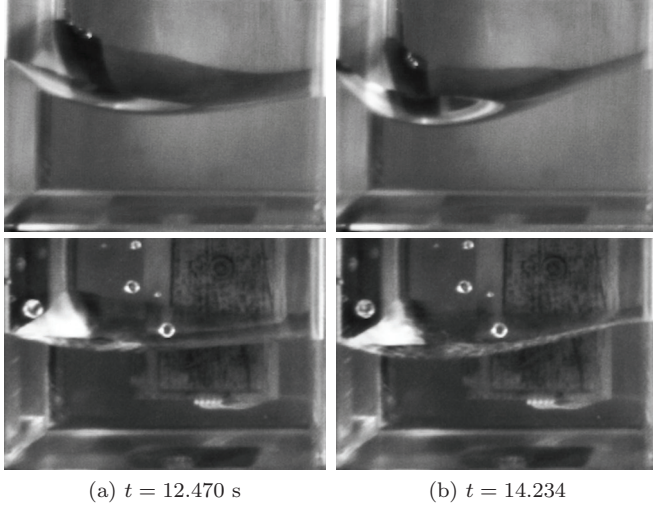


FIG. 8. Snapshots (front views) showing the time evolution of experiments with water a cuboidal container when vibrated in the second resonant mode. The upper rows show the reference cell, while the lower rows show the results of vibrating at  $f = 215.4$  Hz and  $v_\eta = 49.19$  mm/s, corresponding to an applied voltage of 100 V.

the same moment. The vibrated cell is excited in the second resonant mode of the beam at  $f = 215.4$  Hz using a 100-V signal that provides a vibrational velocity  $v_\eta = 49.14$  mm/s.

The second resonant mode [see Fig. 3(c)] has, on average, a more vertical orientation of the vibrational axis. This is consistent with the observed vibroequilibria, which possess a flatter surface compared to the reference experiment. We note that the velocities obtained are approximately half those achieved for the first resonance at the same applied voltage [27], so the vibroequilibria effect is smaller.

### C. Comparison with theory

Using the solutions shown in Fig. 7(a)–7(c), the vibroequilibria effect is characterized by the “front” and “rear” contact points in the midplane (see Fig. 3) parallel to the beam direction ( $x$  axis). These points,  $h_{\text{rear}}$  and  $h_{\text{front}}$ , are located by manually processing the video frames, with an estimated accuracy of  $\pm 1$  pixel. With a spatial resolution of 7.4 pixels/mm in the vertical direction [27], this gives an uncertainty in  $h$  of approximately  $\pm 0.14$  mm. The image contrast is enhanced via local histogram equalization over the regions of interest.

The dimensionless difference between these contact points is calculated as

$$\Delta\mathcal{H} = \frac{h_{\text{rear}} - h_{\text{front}}}{L}, \quad (13)$$

where  $L = 30$  mm is the container size, and shown in Fig. 9 versus  $\eta$ , which is proportional to the square of applied velocity [see Eq. (11)]. Error bars show the estimated uncertainty in the dimensionless difference  $\Delta\mathcal{H}$  of 0.01. This figure confirms that the vibroequilibria effect is proportional to  $\eta$  at leading order, as predicted theoretically in Sec. III A; the curvature can be attributed primarily to the slight variation of the axis of linear velocity  $v_\eta$  with forcing amplitude, which occurs for this mode.

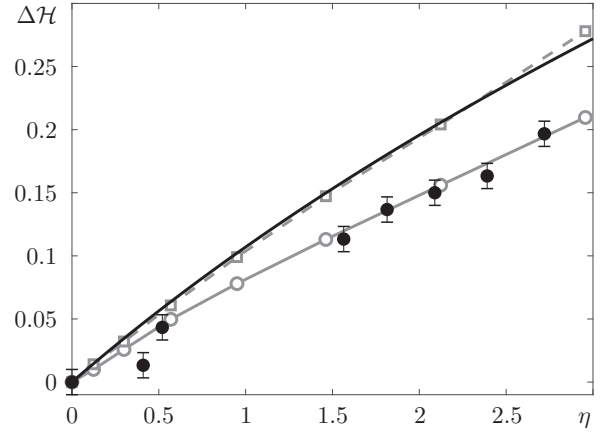


FIG. 9. Comparison of experimental results (solid black dots) with direct numerical simulation of Eqs. (2)–(5) (open gray circles with solid fitting curve), with analogous simulations that ignore the rotational motion (open gray squares with dashed fitting curve), and with the predictions of vibroequilibria theory based on the minimization of Eq. (10) (solid black curve). The contact angle used in these calculations is  $50^\circ$ , while the residual gravity is set to a representative value of  $g_z = 0.05 g_0$ .

The experimental results are also compared in Fig. 9 with the theoretical models of Sec. III, including the direct numerical simulation of the vibrated problem (open gray circles) and the prediction from the energy-functional formulation of vibroequilibria theory (solid black curve). In both cases, the forcing frequency  $f = 79.8$  Hz is that of the first resonant mode, the contact angle  $\beta$  between water and PMMA is taken to be  $50^\circ$  [36], the residual gravity is set to the representative value of  $g_z = 0.05 g_0$  (giving  $\text{Bo} = 6.1$ ), and the remaining parameters are as in Table I except for the viscosity, which is increased to 200 cSt to discourage large-amplitude surface waves and drop ejection. The influence of these last two parameters can be inferred from Fig. 10, which shows the result of several numerical simulations (including rotational motion) with different values of [Fig. 10(a)] viscosity and [Fig. 10(b)] gravity level.

The vibroequilibria effect does not depend on viscosity at leading order and this is confirmed in Fig. 10(a). As seen from these simulations with  $\nu = 10$  cSt, 50 cSt, and 200 cSt (see also Ref. [22]), viscosity does not appreciably affect the final (average) positions of the contact points but does have a clear effect on the relaxation time and on the amplitude of secondary surface waves. The value of 200 cSt was chosen to safely avoid the numerically problematic drop ejection that was frequently observed in the experiments (see Figs. 7 and 8).

The residual gravity level, on the other hand, is clearly an important parameter that broadly acts to suppress the vibroequilibria effect. It varies both during and across experimental runs (see Fig. 5). We selected  $g_z = 0.05 g_0$  for the simulations partly because this is the level achieved in typical parabolic flights. More importantly, better agreement was found for  $g_z = 0.05 g_0$  than for lower values because the vibroequilibria were more nearly symmetric (in  $y$ ) when  $|g_z| > |g_y|$ , making

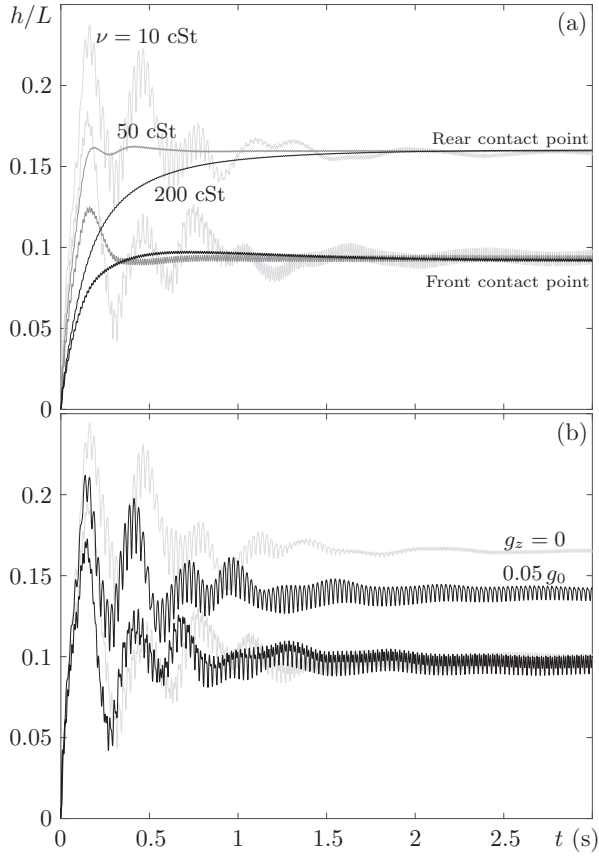


FIG. 10. Influence of viscosity and gravity level for a fixed voltage  $V = 50$  V,  $\eta = 0.57$  on the predicted contact point separation used to quantify the vibroequilibria effect. (a) Simulations of the Navier-Stokes equations with  $g_z = 0.01 g_0$  and  $\nu = 10$  cSt (light gray curves),  $50$  cSt (medium gray curves), and  $200$  cSt (black curves). (b) Simulations using  $\nu = 10$  cSt with  $g_z = 0$  (light gray curves) and  $g_z = 0.05 g_0$  (black curves). The remaining parameters are as in Fig. 9.

the two-dimensional assumption more tenable; the average microgravity level for the data used in Fig. 9 is close to  $g_z = 0.05 g_0$ . We note that, as shown in Fig. 10(b), the front contact point is nearly independent of the gravity level, recalling its weak dependence on forcing, and residual gravity, in the experiment (see Fig. 7).

The Navier-Stokes simulations include the full  $(x, z)$  motion (acceleration) of the container as measured on ground by an accelerometer and gyroscope attached to the side of the container. These measurements are shown in Fig. 11. The commercial software COMSOL MULTIPHYSICS is used to solve the governing equations in two dimensions, corresponding to the midplane  $y = 0$ . The initial conditions  $\mathbf{u} = 0$  at  $t = 0$  are evolved, using a maximum time step of  $1/(10f)$ , until a steady state is reached.

The procedure prescribed by vibroequilibria theory is implemented in a two-dimensional rectangular domain, as in Ref. [22]. We use MATLAB to minimize Eq. (10) over permitted surface configurations using the boundary element method and expand the surface  $z = F(x)$  in terms of basis functions

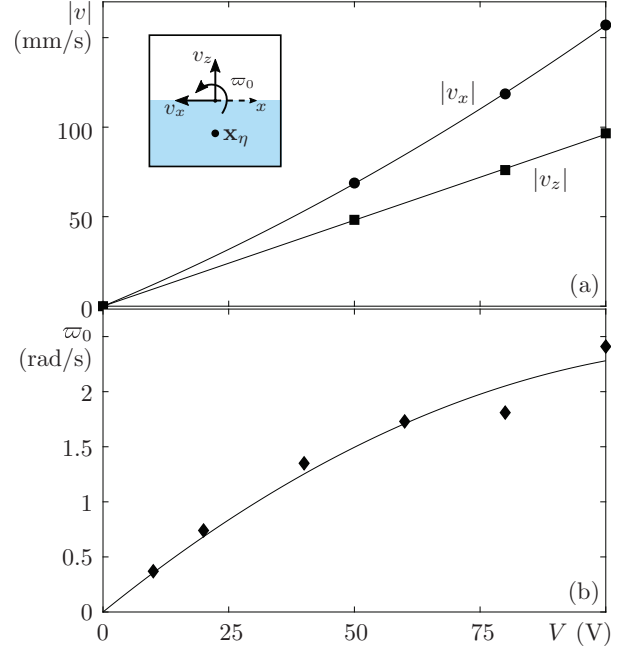


FIG. 11. Measurements (performed on ground) of the maximum linear and angular velocities at the center of the side wall for the first resonant mode. (a) Horizontal velocity  $|v_x|$  (solid dots) and vertical velocity  $|v_z|$  (solid squares). (b) Angular velocity  $\omega_0$ .

$P_n(x)$  that are taken to be Legendre polynomials:

$$F(x) = \sum_{n=0}^N a_n P_n(x). \quad (14)$$

This yields a functional  $\mathcal{L}\{a_n\}$  that can be minimized over a finite set of coefficients.

Since the vibroequilibria theory neglects rotational terms, we use the linear acceleration of the point  $\mathbf{x}_\eta$  in the middle of the unperturbed liquid (assuming it occupies the bottom half of the container; see the inset of Fig. 11) for this calculation. For consistency, the estimated acceleration of this point is also used to calculate  $\eta$  for the experimental data points and the Navier-Stokes simulations. The absence of rotational acceleration in the vibroequilibria calculation leads to an error since the real motion [see Fig. 3(b)] is not purely linear, particularly in the case of the first resonant mode. From Fig. 11, this error is expected to be on the order of 20–30%; that estimate follows from multiplying  $\omega_0$  by 20 mm, which is half the length, and comparing with  $|v|$ . To confirm that this is the principal source of error, the Navier-Stokes simulations were repeated without rotational terms (open gray squares in Fig. 9) and found to be in excellent accord with the vibroequilibria calculations.

Overall, the experimental results provide a clear confirmation of the vibroequilibria effect in microgravity. There is convincing agreement between the predicted and the observed position of the fluid over the considered forcing range  $\eta \lesssim 3$  despite the simplifying assumptions made in the calculations, which include neglect of the lateral ( $y$ ) dimension to justify a two-dimensional model, the use of constant residual gravity and, in the case of vibroequilibria theory, the approximation



of linear container motion. This latter error is noticeable for the excitation used here but could be accounted for with an alternative separation of timescale approach that does not assume potential flow.

Although further comparison with vibroequilibria theory may be possible, the above issues, as well as the variation of the effective Bond number during the parabolic flight, make this difficult. The available vibrational amplitude was an additional limitation. For example, according to the results of Fernández *et al.* [22], the liquid was deep enough ( $d/L \simeq 0.5 > 0.36$ ) to undergo a sudden transition from a symmetric to an asymmetric solution. However, not only were the vibroequilibria solutions in the experiment not symmetric in  $x$ , since even the principal component of the acceleration was oblique, but the predicted amplitude ( $\eta \sim 15$ ) for this (saddle-node) transition was not reached.

## VI. CONCLUSIONS

Results from microgravity experiments investigating the vibroequilibria effect in cylindrical and cuboidal containers partially filled with water or silicone oil have been presented and discussed. The experiments utilized different resonance modes of a cantilever beam excited by a pair of piezoelectric ceramics controlled by an applied ac voltage. The resulting motion was generally oblique to the initial fluid surface and “more vertical” for the second resonant mode compared to the first. Each excited cell was compared to an unforced reference cell with the same liquid configuration that experienced only residual gravity. The experimental results confirm the predicted “gravity-like” tendency of vibroequilibria solutions to move large portions of the surface into a more perpendicular orientation with respect to the (average) vibrational axis. For the first resonance mode, this led to the formation of a dip or crater in the interior, with the rear (and sometimes front) contact line climbing upward. For the second resonance mode, this led to a flattening of the surface compared to the unforced reference cell.

These experimental results provide clear evidence of the vibroequilibria effect in both containers and with both liquids. Although observed long ago on ground [8,11] and even in microgravity [25], this is the first experiment that the authors

are aware of to quantify the vibroequilibria effect and to compare the observed amplitude of solutions directly with numerical simulations of the Navier-Stokes equations and with calculations using the more recently developed vibroequilibria theory, which relies on a separation of timescales [19–21]. An analogous experiment on ground would be hampered by the large amplitudes required and, with that, the simultaneous excitation of other dynamical modes.

In the CFVib experiment, in fact, drop ejection from large-amplitude surface waves was often observed in the case of water and 5-cSt silicone oil, and excessive drop ejection sometimes prevented the vibroequilibria effect from being clearly measured. However, despite the presence of a small number of drops, the cuboidal containers with water provided good results that allowed for a clear quantitative comparison with direct numerical simulations and with theory. The agreement demonstrates, experimentally, the validity of the vibroequilibria theory and shows that it can be used to accurately predict the position of fluids in microgravity.

With appropriate container design and choice of excitation (here determined by the resonance modes of the beam), it should be possible to use the vibroequilibria effect for control and management of fluids in microgravity environments. Aside from this consideration, the amplification of the vibroequilibria effect in weightlessness, where the reorientation is countered only by surface tension and contact forces, means that it should be taken into consideration whenever sufficient vibrations, known as *g-jitter* [37], are present.

## ACKNOWLEDGMENTS

This work was supported by the European Space Agency (ESA) Education Office Fly Your Thesis! programme, the 65th ESA Parabolic Flight Campaign, and the Ministerio de Economía y Competitividad under Projects No. ESP2013-45432-P and No. ESP2015-70458-P. We also acknowledge the essential contributions of ELGRA, Novespace, E-USOC, and the ETS de Ingeniería Aeronáutica y del Espacio during the project. Finally, we thank Trenz Electronic for their Analog Discovery device, Analog Devices for providing the accelerometers, and Krytox Performance Lubricants (The Chemours Company) for supplying the vacuum oil.

- 
- [1] Y. Ito and S. Komori, *AIChE J.* **52**, 3011 (2006).
  - [2] J. Miles and D. Henderson, *Annu. Rev. Fluid Mech.* **22**, 143 (1990).
  - [3] F. Varas and J. M. Vega, *J. Fluid Mech.* **579**, 271 (2007).
  - [4] C. J. R. Garrett, *J. Fluid Mech.* **41**, 837 (1970).
  - [5] B. J. S. Barnard and W. G. Pritchard, *J. Fluid Mech.* **55**, 245 (1972).
  - [6] A. F. Jones, *J. Fluid Mech.* **138**, 53 (1984).
  - [7] I. Tinao, J. Porter, A. Laverón-Simavilla, and J. Fernández, *Phys. Fluids* **26**, 024111 (2014).
  - [8] M. Faraday, *Philos. Trans. R. Soc. Lond.* **121**, 299 (1831).
  - [9] T. B. Benjamin and F. Ursell, *Proc. R. Soc. Lond. A* **225**, 505 (1954).
  - [10] K. Kumar and L. S. Tuckerman, *J. Fluid Mech.* **279**, 49 (1994).
  - [11] G. H. Wolf, *Z. Phys.* **227**, 291 (1969).
  - [12] D. V. Lyubimov and A. A. Cherepanov, *Fluid Dyn. Res.* **21**, 849 (1986).
  - [13] E. Talib, S. V. Jalikop, and A. Juel, *J. Fluid Mech.* **584**, 45 (2007).
  - [14] D. Beysens, Y. Garrabos, D. Chatain, and P. Evesque, *Eurphys. Lett.* **86** (2009).
  - [15] T. Lyubimova, A. Ivantsov, Y. Garrabos, C. Lecoutre, G. Gandikota, and D. Beysens, *Phys. Rev. E* **95**, 013105 (2017).
  - [16] V. Shevtsova, Y. A. Gaponenko, V. Yasnou, A. Mialdun, and A. Nepomnyashchy, *J. Fluid Mech.* **795**, 409 (2016).
  - [17] P. Salgado Sánchez, V. Yasnou, Y. Gaponenko, A. Mialdun, J. Porter, and V. Shevtsova, *J. Fluid Mech.* **865**, 850 (2019).
  - [18] P. Salgado Sánchez, Y. A. Gaponenko, J. Porter, and V. Shevtsova, *Phys. Rev. E* **99**, 042803 (2019).



- [19] D. V. Lyubimov, A. A. Cherepanov, T. P. Lyubimova, and B. Roux, *C. R. Acad. Sci. Paris* **325**, 391 (1997).
- [20] K. Beyer, I. Gawriljuk, M. Günther, I. Lukovsky, and A. Timokha, *Z. Angew. Math. Mech.* **81**, 261 (2001).
- [21] I. Gavriljuk, I. Lukovsky, and A. Timokha, *Z. Angew. Math. Phys.* **55**, 1015 (2004).
- [22] J. Fernández, I. Tíno, J. Porter, and A. Laverón-Simavilla, *Phys. Fluids* **29**, 024108 (2017).
- [23] J. M. Perez-Gracia, J. Porter, F. Varas, and J. M. Vega, *J. Fluid Mech.* **739**, 196 (2014).
- [24] P. Salgado Sánchez, J. Porter, I. Tíno, and A. Laverón-Simavilla, *Phys. Rev. E* **94**, 022216 (2016).
- [25] R. F. Ganiev, V. D. Lakiza, and A. S. Tsapenko, *Sov. Appl. Mech.* **13**, 499 (1977).
- [26] D. Beysens, *Europhys. News* **37**, 22 (2006).
- [27] J. Fernandez, P. Salgado Sánchez, I. Tíno, J. Porter, and J. M. Ezquerro, *Microgravity Sci. Technol.* **29**, 351 (2017).
- [28] V. Pletser, S. Rouquette, U. Friedrich, J.-F. Clervoy, T. Gharib, F. Gai, and C. Mora, *Microgravity Sci. Technol.* **28**, 587 (2016).
- [29] Novespace, <https://www.airzerog.com/novespace-and-avico/>.
- [30] L. D. Landau and E. M. Lifshitz, *Fluid Mechanics*, 2nd ed., Course of Theoretical Physics Vol. 6 (Pergamon Books Ltd., London, 1987).
- [31] A. J. James, M. K. Smith, and A. Glezer, *J. Fluid Mech.* **476**, 29 (2003).
- [32] A. J. James, B. Vukasinovic, M. K. Smith, and A. Glezer, *J. Fluid Mech.* **476**, 1 (2003).
- [33] S. Douady, S. Fauve, and O. Thual, *Europhys. Lett.* **10**, 309 (1989).
- [34] P. Salgado Sánchez, Y. Gaponenko, V. Yasnou, A. Mialdun, J. Porter, and V. Shevtsova, *J. Fluid. Mech.* (to be published).
- [35] Y. Li and A. Umemura, *J. Fluid Mech.* **759**, 73 (2014).
- [36] X. Zhao, J. Cheng, S. Chen, J. Zhang, and X. Wang, *Colloid Polym. Sci.* **288**, 1327 (2010).
- [37] E. S. Nelson, An examination of anticipated g-jitter on space station and its effects on materials processes, Technical Report No. 103775, NASA Lewis Research Center, 1994.